ISPRS Journal of Photogrammetry and Remote Sensing 230 (2025) 804–819

Contents lists available at ScienceDirect

ISPRS Journal of Photogrammetry and Remote Sensing

journal homepage: www.elsevier.com/locate/isprsjprs

A novel 3D model for joint estimation of the repositioning and tilting error in GPRI-II terrestrial radar interferometry

Yuhao Liu [a], Zeyu Zhang [a], Songbo Wu [a,b,*], Xiaoli Ding [a,b,c], Guoqiang Shi [a,b,c], Zhendong Zhang [a], Mahmoud Abdallah [a,d], Bochen Zhang [e]

[a] Department of Land Surveying and Geo-Informatics, The Hong Kong Polytechnic University, Hong Kong, China
[b] Research Institution for Land and Space, The Hong Kong Polytechnic University, Hong Kong, China
[c] Shenzhen Research Institute, The Hong Kong Polytechnic University, Shenzhen, China
[d] Public Works Department, Mansoura University, Mansoura, Egypt
[e] MNR Key Laboratory for Geo-Environmental Monitoring of Great Bay Area, College of Civil and Transportation Engineering, Shenzhen University, Shenzhen, China

ARTICLE INFO

Keywords:
Discontinuous Ground-based interferometric radar application
GPRI-II
Instrument reconfiguration
Repositioning error
Tilting error
Upper bounds of error tolerance

ABSTRACT

Long-term deformation monitoring with ground-based interferometric radar (GBIR), such as the GPRI-II, is often conducted with a discontinuous strategy, i.e., discontinuous GBIR, which requires repeated instrument setup. While prior studies have addressed repositioning errors during this process by correcting phase ramps, it is difficult to provide parameters essential for instrument reconfiguration. This paper introduces a novel 3D model to estimate and correct re-setup errors for the GPRI-II based on the polar-coordinate geometry frame. The model employs a dual-component approach, separating errors into repositioning (locational changes) and tilting (tilting angle variations) components. A joint estimation model is designed to estimate both errors simultaneously. More important, for the first time, the instrument reconfiguration becomes enabled based on the estimated results from the proposed model. The effectiveness of the proposed model is verified through real-world experiments and compared against existing methods. The results indicate the repositioning-only model achieved the highest accuracy, showing improvements of 16.93 % and 50.48 % in repositioning error correction and 10.87 % and 10.66 % in tilting error correction compared to polynomial fitting and the traditional model, respectively. The joint estimation achieved 30.10 %, 32.58 %, and 48.09 % improvements over the repositioning-only estimation, polynomial fitting, and traditional model. The instrument reconfiguration achieved accuracies of 2.12 mm (horizontal), 1.07 mm (vertical), 0.25° (horizontal angle), 2.02° (tilt direction angle), and 0.17° (tilt angle). In addition, we determine the upper bounds of error tolerance for the system, establishing maximum correctable errors of 0.64 m (horizontal) and 0.30 m (vertical). All the study results highlight the robustness of the proposed model and its potential to significantly enhance the precision of discontinuous GPRI-based deformation monitoring.

1. Introduction

Ground-based interferometric radar (GBIR) is a non-contact and radar-based terrestrial remote sensing technique that can deliver near-real-time deformation monitoring with extensive spatial coverage and high precision (Werner et al., 2008; Monserrat et al., 2014). It obtains the target deformation by analyzing phase differences in radar waves between multiple observations(Kobayashi and Miyahara, 2020). Its accuracy typically ranges from sub-millimeter to a few millimeters, depending on factors such as the characteristics of the targets, the monitoring geometry to the targets, and environmental conditions, mainly the atmospheric delay, etc. (Monserrat et al., 2014). Thanks to its portability and adaptability across diverse settings, GBIR has been widely used for monitoring both natural and man-made structures, including landslides detection(Herrera et al., 2009; Noferini et al., 2007), glacier dynamics (Dematteis et al., 2017; Luzi et al., 2007; Noferini et al., 2009), slope stability in open pit mines (Cao et al., 2021; Liu et al., 2016), dams (Qiu et al., 2020; Xiang et al., 2019), and urban infrastructure (Liu et al., 2025; Zhang et al., 2018).

In practice, GBIR systems can operate in two primary data

* Corresponding author at: Department of Land Surveying and Geo-Informatics, The Hong Kong Polytechnic University, Hong Kong, China.
E-mail address: song.bo.wu@connect.polyu.hk (S. Wu).

https://doi.org/10.1016/j.isprsjprs.2025.10.010
Received 11 May 2025; Received in revised form 20 August 2025; Accepted 10 October 2025
Available online 17 October 2025

acquisition modes: continuous (C-GBIR) and discontinuous (D-GBIR) (Crosetto et al., 2014; Wu et al., 2023). In the C-GBIR mode, instruments are permanently installed at a fixed location to collect data at regular intervals (e.g., every few minutes), ensuring continuous monitoring. However, permanent installations are often impractical due to constraints such as high maintenance costs and environmental factors (Monserrat et al., 2014). In contrast, D-GBIR mode periodically revisits the site (e.g., weekly) for repeated monitoring by temporarily installing instruments for each measurement period (Crosetto et al., 2014). Therefore, D-GBIR is well-suited for long-term monitoring of slow deformations. However, this mode requires the instrument to be precisely re-setup to its original location for each round due to the high sensitivity to the changes in geometry of GBIR (Wolff et al., 2024). Even minor repositioning errors on the order of millimeters can introduce significant errors that can then impact deformation monitoring and subsequent hazard analysis (Wang et al., 2019).

Many studies have been conducted to mitigate the effect of repositioning error during the data processing. They can broadly be divided into two categories. The first constructs a permanent pile to setup the instrument every time in each short-term session to maintain consistent positioning (Izumi et al., 2021; Su et al., 2022). The second group is to estimate the repositioning errors based on the polynomial method (Hu et al., 2021; Wang et al., 2019) and model-constrained fitting (Mo et al., 2024; Yang et al., 2017). However, pile construction is often restricted by local regulations, and repeated installations on the pile can still introduce tilting errors. Methods only reliant on simple phase ramp with polynomial fitting are susceptible to long-wave signal interference, such as atmospheric delay, leading to estimate errors and signal ambiguity (Zhang et al., 2014). In addition, repositioning errors are inherently three-dimensional (3D), involving deviations in multiple spatial directions, a factor largely overlooked by existing methods, thus limiting their effectiveness. Moreover, traditional methods are difficult to provide parameters essential for instrument reconfiguration for each round of monitoring that will hinder their practical utility.

In this study, we propose a novel 3D joint estimation model to parameterize and correct instrument re-setup errors in GPRI-II systems during multiple short-term sessions for long-term deformation monitoring. In this model, a dual-component approach is employed to separate GPRI-II re-setup errors into two components: repositioning (locational changes) and tilting (tilting angle variations). Both error components are modeled within a polar-coordinate geometry framework. We also developed a joint estimation framework to simultaneously estimate these errors. The instrument reconfiguration, for the first time, became enabled in the basis of the proposed model. To evaluate the effectiveness of the proposed method, the real-world experiments were conducted and compared with the existing methods. The derived reconfiguration parameters were verified with the measurements from the total station. Finally, we determined the upper bounds of error tolerance, providing a recommended re-setup error range for practical deployments. The rest of the paper is organized as follows: Section 2 overviews the used GBIR system, and Section 3 introduces the proposed methodology. The experiments are conducted in Section 4. Section 5 provides a discussion of the accuracy, reliability, and limitations of the model. Section 6 gives the conclusion.

2. GPRI-II system and error Source

In this section, we first overview of the GPRI-II GBIR system by detailing its parameters and geometric characteristics, followed by an introduction to the interferometric phase and potential error phase components.

2.1. Overview of the GPRI-II system

The GAMMA Portable Radar Interferometer (GPRI) is a ground-based real-aperture radar system with rotating antennas operating at Ku-band with 17.2 GHz (Werner et al., 2008). As presented in Fig. 1 (a), it consists of a transmit antenna and two receiving antennas (the beamwidths in azimuth and elevation are 0.4 degrees and 45 degrees, respectively), an antenna bracket with a GPS antenna on the top center to provide geographic coordinates and time information (decimeter-level accuracy, with Coordinated Universal Time), a radio frequency (RF) assembly, mounted on the bracket to generation the linear frequency modulation chirp and obtains the range compressed radar echo, an azimuth positioner which can undertake panoramic scanning (360 degrees), a tripod, an instrument computer, and a battery pack.

GPRI-II is equipped with two imaging modes: Fixed Azimuth Scanning (FAS) mode, and Rotated Azimuth Scanning (RAS) mode. In RAS mode, the radar beam scans the front sector by rotating the antennas along the azimuth direction, enabling panoramic monitoring, as shown in Fig. 1(b). This mode allows monitoring of targets from 50 m to 10 km

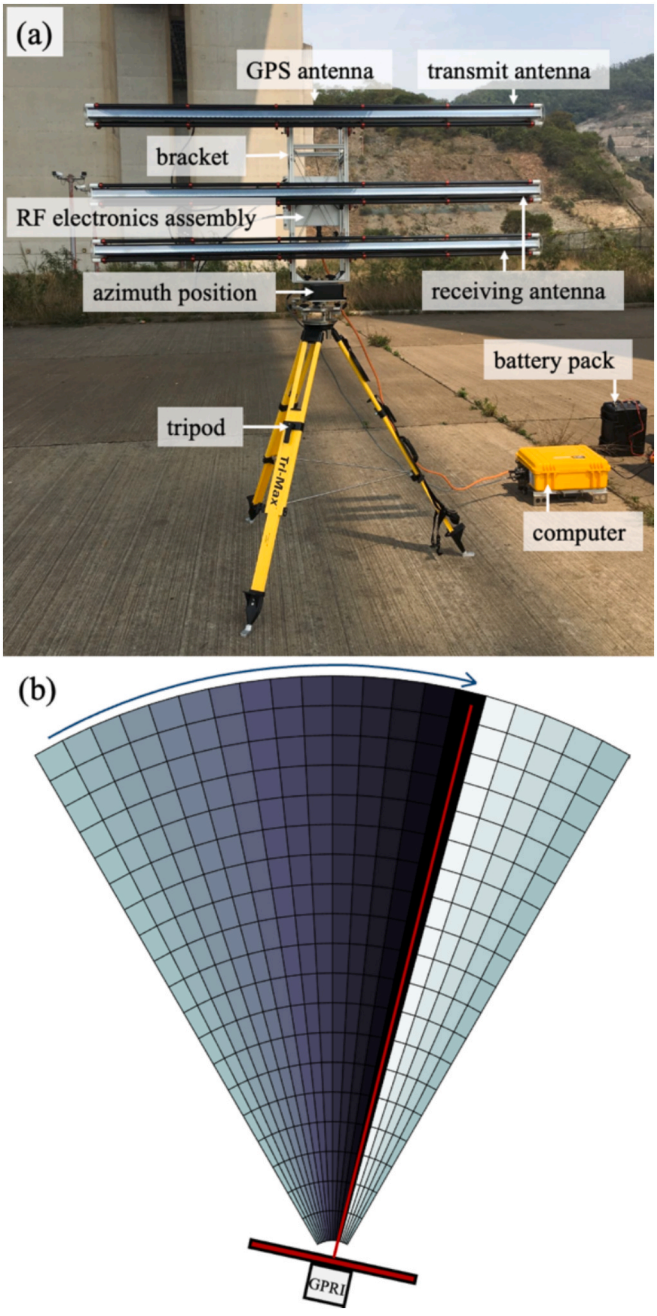

Fig. 1. GPRI-II system and observation geometry. (a) GAMMA portable radar interferometry (b) observation geometry of RAS mode.

and provides two-dimensional (2D) images with a range resolution of 0.75 m and an azimuth resolution of 6.8 m at 1 km (Werner et al., 2008). In this study, we mainly focus on the observation from the RAS mode to correct the errors during the instrument re-setup. The technical specifications of the GPRI-II RAS mode are detailed in Table 1.

2.2. Interferometric phase and error sources

The interferometric technique can be implemented with the GBIR system for the deformation monitoring (Monserrat et al., 2014). In contrast to spaceborne InSAR, GBIR offers a simplified approach, as the topographic phase (ϕ_{topo}) and flat-earth phase (ϕ_{flat}), are generally negligible due to the fixed observational geometry of the GBIR systems (Zhang et al., 2018). Following co-registration of two GBIR images acquired at different time, a step often obviated when the instrument maintains a consistent geometric configuration, the images conjugation is then conducted to achieve the interferometric phase (ϕ), which is composed of the deformation signal (ϕ_{defo}), atmospheric delay phase (ϕ_{atmo}), and residual noise (ϕ_{noise}) (Monserrat et al., 2014).

$$\phi = \phi_{defo} + \phi_{atmo} + \phi_{noise} \tag{1}$$

When we conduct the D-GBIR application for long-term deformation monitoring, the GBIR is required to re-setup on the same position, which will invariably induce changes in the instrument attitude and introduce additional phase components (Yang et al., 2017). For instance, in the case of the GPRI-II instrument, the phase contributions arising from such re-setup can be categorized into two components: the repositioning error (ϕ_{repo}) associated with inaccuracies in the instrument position in three dimensions (3D), and the tilting error (ϕ_{atti}) resulting from changes in the tilting angle. Under these conditions, the interferometric phase in Eq. (1) can be extended as:

$$\phi = \phi_{defo} + \phi_{repo} + \phi_{tilt} + \phi_{atmo} + \phi_{noise} \tag{2}$$

As shown in Eq. (2), re-setup errors create additional phase in the observation, causing inaccuracies at the final deformation result if without the correction. Generally, the re-setup errors are presented as the phase fringes (Su et al., 2022). Dense fringes can lead up to centimeter error in deformation, even can cause the decorrelation and errors in phase unwrapping during the data processing. Several studies have developed methods to address errors from instrument re-setup, but these methods typically focus on correcting phase ramps using specific equations of phase-ramp, e.g., polynomial fitting method (Hu et al., 2021; Wang et al., 2019). However, such approaches are incapable of providing the parameters necessary for instrument reconfiguration. In addition, re-setup errors are distributed across multiple directions, leading to diverse phase changes that are challenging to model and correct using a simple phase-ramp approach (Yang et al., 2017). Utilizing such models may leave significant residual errors in the final deformation results. To overcome these limitations and improve error correction, we aim to propose a new error model based on a polar coordinate system, using the observation geometry of the GPRI-II RAS mode. The proposed model will consider both repositioning errors and tilting errors, offering a complete approach to modeling and correcting re-setup errors even support for the instrument reconfiguration.

Table 1
Technical characteristics of the GPRI-II RAS mode.

Parameters	Values
Developer	GAMMA
Radar type	FMCW
Central frequency	17.2 GHz (Ku-band)
Bandwidth	200 MHz
Polarization	VV
Measurement range	50 m to 10,000 m
Spatial resolution (range × azimuth)	0.75 m × 6.8 m @ 1 km
Accuracy	Millimeter-level
Rotating speed	0.1 °/s to 10 °/s
Elevation angle	−45 ° to 45 °

3. Proposed methodology

This section introduces the proposed joint estimation methodology from three aspects: First, we introduce the geometry model of repositioning error and tilting error, respectively, according to the polar coordinates. Then, we design a joint estimation procedure that is used to estimate both errors simultaneously.

3.1. Model of repositioning error

Given that the repositioning error of the instrument manifests as a three-dimensional (3D) discrepancy, while the phase observations in GPRI are constrained to a single-dimensional line-of-sight (LOS) direction. To derive 3D coordinates from one-dimensional observations poses significant challenges, therefore, we established the geometric model of repositioning error within a polar coordinate system of the RAS mode geometry to better capture the spatial relationships and facilitate the analysis of the error components.

As shown in Fig. 2(a), the initial position of the radar O is set as the coordinate origin, and the horizontal direction of the radar reaching the target pixel as the coordinate axis, then the coordinates of GPRI $O(0, 0, 0)$ and the target pixel $P\left(\sqrt{R^2 - H^2}, 0, H\right)$ are obtained, where R and H are slant distance and relative height between radar and target, respectively. It is worth noting that the GPRI is capable of retrieving a DEM using an interferogram generated from upper and lower antennas, which then can be used to determine the relative height, as shown in Eq. (3) (Werner et al., 2008),

$$H = -\frac{\lambda^2}{8\pi^2 B_p}\phi^2 - \frac{\lambda R}{2\pi B_p}\phi + \frac{B_p}{2} \tag{3}$$

where λ and B_p are wavelength and perpendicular baseline.

In this polar system, we define the the component of the baseline parallel to the horizontal plane as the horizontal baseline B_{hr}, and the component perpendicular to the horizontal plane as the vertical baseline B_{vr}. When the GPRI-II system is re-setup on point A, the coordinate of GPRI-II can be defined as $A(B_{hr}, \theta_{hr}, B_{vr})$, in which B_{hr} is the displacement along the horizontal direction, and B_{vr} is the displacement along vertical direction. θ_{hr} is horizontal angle from start angle of scanning to horizontal baseline direction. The line connecting O and A represents the spatial baseline B_{repo} between two observations taken from different positions. Therefore, the contribution of the repositioning error component for target P in the LOS direction can be expressed as the projection of the spatial baseline in the LOS direction, which is the parallel baseline $B_{\|}$.

$$\phi_{repo} = -\frac{4\pi}{\lambda}B_{\|} = -\frac{4\pi}{\lambda}B_{repo}\cos\theta_{proj} \tag{4}$$

The geometric relationships between baseline B_{repo} and projection $B_{\|}$ can be characterized by the cosine theorem, which is only applicable in the rectangular coordinate system. Under the rectangular coordinate system, vector $\overrightarrow{OP}$ and $\overrightarrow{OA}$ can be expressed as

$$\begin{cases} \overrightarrow{OP} = \left(0,\ \sqrt{R^2 - H^2},\ H\right) \\ \overrightarrow{OA} = (B_{hr}\sin\theta_{hr}, B_{hr}\cos\theta_{hr}, B_{vr}) \end{cases} \tag{5}$$

then the cosine of projection angle θ_{proj} expressed as follow.

$$\cos\theta_{proj} = \frac{\overrightarrow{OP} \bullet \overrightarrow{OA}}{\left|\overrightarrow{OP}\right|\left|\overrightarrow{OA}\right|} = \frac{\sqrt{R^2 - H^2}B_{hr}\cos\theta_{hr} + HB_{vr}}{RB_{repo}} \tag{6}$$

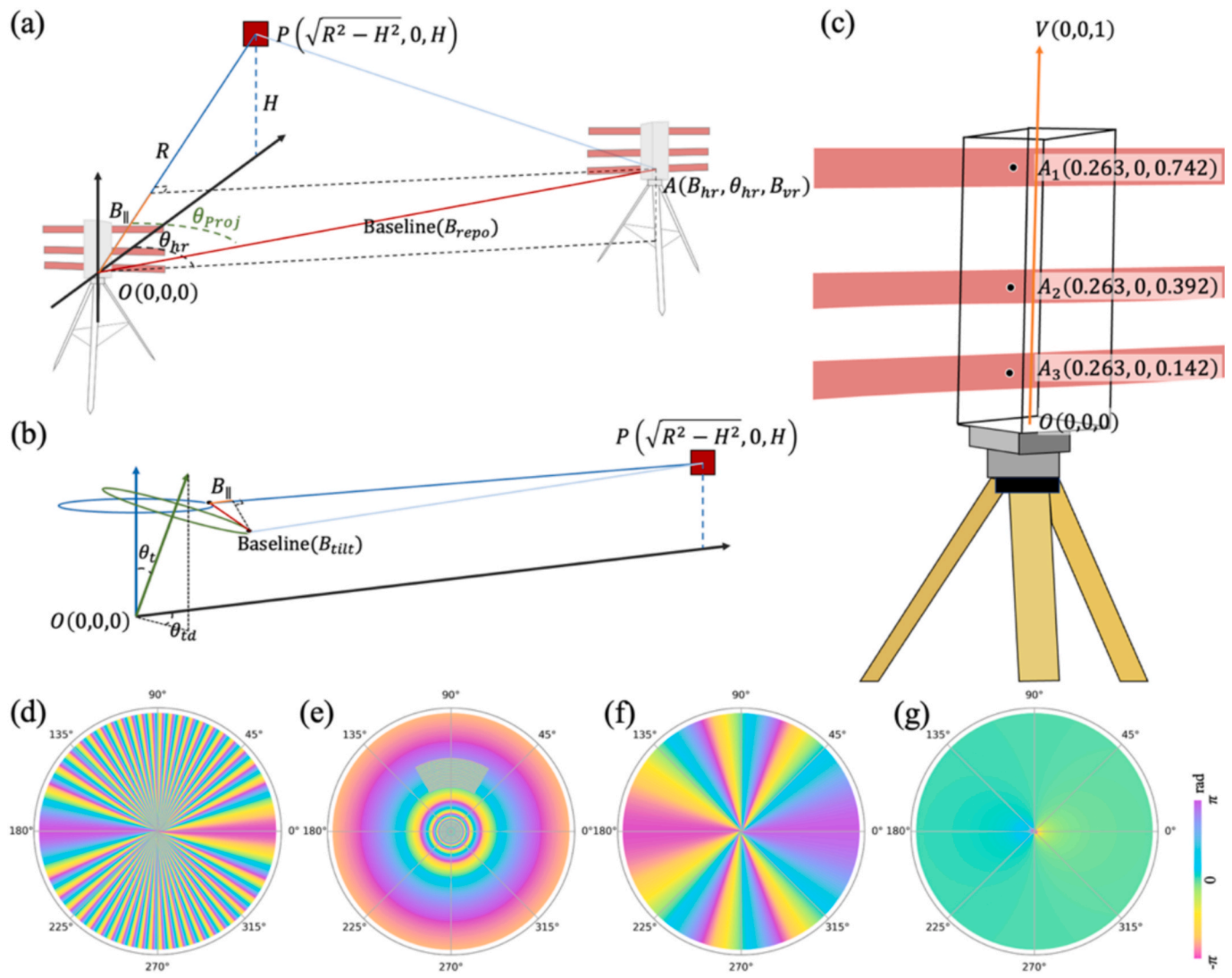

Fig. 2. The geometry of GPRI-II and its re-setup error correction model. (a) monitoring geometry at different locations (b) monitoring geometry with different tilt angles (c) geometric position of the radar antenna centers on the bracket (d) spatial pattern of the horizontal component in repositioning error (e) spatial pattern of vertical component in repositioning error (f) spatial pattern of the horizontal component in tilting error (g) spatial pattern of vertical component in tilting error.

Combining Eq. (5) and Eq. (6), the repositioning error phase can be expressed as Eq. (7).

$$\phi_{repo} = -\frac{4\pi}{\lambda}\left(\frac{\sqrt{R^2-H^2}}{R}B_{hr}\cos\theta_{hr}+\frac{H}{R}B_{vr}\right) \tag{7}$$

It can be seen from the Eq. (7), the repositioning error phase can be divided into horizontal component $-\frac{4\pi}{\lambda}\frac{\sqrt{R^2-H^2}}{R}B_{hr}cos\theta_{hr}$ and vertical component $-\frac{4\pi}{\lambda}\frac{H}{R}B_{vr}$.

To illustrate these two components in detail, we have simulated their spatial patterns based on the proposed formula. In Fig. 2(d), we set $B_{hr} = 0.1\,m$ and $B_{vr} = 0\,m$ to simulate the horizontal component within a 300-meter observation radius. The horizontal component can be expressed as $\frac{4\pi}{\lambda}\frac{\sqrt{R^2-H^2}}{R}B_{hr}cos\theta_{hr}$, which is low at 0° and 180° but high at 90° and 270°. The corresponding illustrate can be found in Fig. 2(d), where the interferometric fringes are sparsely distributed at 0° and 180° but densely packed at 90° and 270°. In Fig. 2(e), we set $B_{vr} = 1\,m$ and $B_{hr} = 0\,m$, and the relative height $H = 1\,m$ to simulate the vertical component. In addition, we introduce a slope with a coefficient of 1, where the elevation increases with distance from 60° to 120°, to obtain the vertical component. The fringes become sparser as the distance increases, and if a slope is present, they will align with the terrain, resembling contour lines.

3.2. Model of tilting error

Tilting error is a consequence of discrepancies in the tilting angles of the antenna bracket (see Fig. 2b). Due to the inherent coupling between azimuth position and bracket tilt, such errors are virtually unavoidable (Noll and Rydlund, 2020). Although a bubble level typically used for tilt calibration during each radar installation, it remains challenging to achieve consistent angle alignment due to the limited precision of the leveling tool (Luo et al., 2018). Consequently, tilting errors can occur regardless of whether the GPRI-II is mounted on a tripod or a monitoring pile.

The tilting error in a fixed GPRI-II installation can be represented by the tilt direction angle θ_{td} and tilt angle θ_t, as illustrated in Fig. 2(b). Based on θ_{td} and θ_t, the corresponding rotation axis vectors of the antenna bracket can be determined. Then, according to the geometric

structure of the bracket, the coordinates of the antenna centres can be calculated. The baseline parameters are defined as the coordinate differences of the antenna centres under each scanning angle. These baseline parameters can be subsequently used to compute the tilting error phase.

The model of titling error is estimated under the polar coordinates system. The center of the bracket base is defined as the coordinate origin, and the forward direction of the GPRI-II is set as the coordinate axis as shown in Fig. 2(b). To reduce computational complexity and improve the robustness of estimation, the reference rotation axis vector is assumed as $V_0(0,0,1)$. Under this assumption, other rotation axis vectors can be represented as $V(sin\theta_t cos\theta_{td}, sin\theta_t sin\theta_{td}, cos\theta_t)$.

Based on the geometric structure of the antenna bracket, see Fig. 2 (c), the coordinates of the antenna geometry centres along the defined axis direction can be denoted as $A_{i,j,k}$, where i, j, and k denote the indices of different tilt angles, scanning azimuth angles, and antenna, respectively. The coordinates of the antenna geometry centres can be represented as Eq. (8).

$$\begin{cases} A_{0,0,upper} = (0.263, 0, 0.742) \\ A_{0,0,lower} = (0.263, 0, 0.142) \\ A_{1,0,upper} = A_{0,0,upper} + 0.742(V - V_0) \\ A_{1,0,lower} = A_{0,0,lower} + 0.142(V - V_0) \end{cases} \tag{8}$$

Based on the Rodrigues' rotation formula (Rodrigues, 1840), the coordinates of the antenna centers at any other angle can be calculated, as expressed in Eq. (9).

$$A_{i,\bullet,k} = A_{i,j,k}\cos\theta_r + (V_i \times A_{i,j,k})\sin\theta_r + V_i(V_i \times A_{i,j,k})(1 - \cos\theta_r) \tag{9}$$

where θ_r is represented as the scanning angle, defined as the angle between the scanning direction and the coordinate axis.

The baseline B_{tilt} is represented as the spatial distance between two antenna center coordinates corresponding to the same target, as Eq. (10).

$$B_{tilt} = A_{1,\bullet,k} - A_{0,\bullet,k} \tag{10}$$

Due to the small difference in tilt angle, it can be assumed that targets at the same scanning angle θ_r remain consistent in different status indexes of the rotation axis after registration. Then the baseline B_{tilt} can be decomposed into horizontal and vertical components, denoted as B_{ht}, and B_{vt}, respectively, as shown in Eq. (11).

$$\begin{cases} B_{vt} = \left(\dfrac{B_{tilt} \bullet V_i}{\|V_i\|^2}\right) V_i \\ B_{ht} = B_{tilt} - B_{vt} \end{cases} \tag{11}$$

It should be noted that the baseline parameters corresponding to each azimuth angle j° are different. Substituting the sets of horizontal baselines B_{ht}, horizontal baseline projection angles θ_{Proj}, and vertical baselines B_{vt} into the repositioning error model, the tilting error phase then can be obtained with Eq. (12).

$$\phi_{tilt} = -\frac{4\pi}{\lambda}\left(\frac{\sqrt{R^2 - H^2}}{R} B_{ht}\cos\theta_{Proj} + \frac{H}{R} B_{vt}\right) \tag{12}$$

In the tilting error model, the horizontal baseline is significantly larger than the vertical baseline in the tilting error model due to the near-vertical rotation axis and small tilt angle, therefore, the horizontal component is generally dominant. The spatial pattern for a 1° tilt in the tilting error model is shown in Fig. 2(f) and Fig. 2(g). Although the horizontal and vertical spatial distributions are similar to the repositioning error model, the fringe density exhibits significantly reduced variations. In addition, since changes in tilt angle cause larger displacements at the upper antenna, the resulting error phases are generally more pronounced for the upper antenna compared to the lower one.

3.3. Joint estimation model

In the practical applications, the GPRI-II system is typically conducted using a tripod, which will introduce both repositioning and tilting errors. As stated in the previous sections, although the spatial patterns are similar, the magnitude and horizontal angle are typically different. Moreover, repositioning and tilting errors often coexist. For instance, tilting errors may be introduced when the orientation of radar is altered due to re-install, while adjustments to the tilt angle can shift the rotation center of the azimuth position structure, thereby inducing a slight repositioning error. Relying on a single-error model to correct the phase error may result in incomplete error removal and inaccurate estimation of reconfiguration parameters. Therefore, a joint estimation is necessary to compensate for these two types of errors, represented as Eq. (13).

$$\begin{aligned} \phi_{joint} &= \phi_{Repo} + \phi_{tilt} \\ &= -\frac{4\pi}{\lambda}\left[\frac{\sqrt{R^2 - H^2}}{R}\left(B_{hr}\cos\theta_{hr} + B_{ht}\cos\theta_{proj}\right) + \frac{H}{R}\left(B_{vr} + B_{vt}\right)\right] \end{aligned} \tag{13}$$

Consider a system of linear observation equations with 3 and 2 real-valued unknown parameters in repositioning and tilting components, respectively, including horizontal baseline B_{hr}, azimuth angle θ_h, vertical baseline B_{vr}, tilt direction angle θ_{td}, and tilt angle θ_t. The equation for each pixel is given in Eq. (14).

$$\begin{bmatrix} \phi_1 \\ \phi_2 \\ \vdots \\ \phi_n \end{bmatrix} = -\frac{4\pi}{\lambda}\left(\begin{bmatrix} a_1 \\ a_2 \\ \vdots \\ a_n \end{bmatrix}^T \begin{bmatrix} \cos\theta_{hr_1} B_{hr} + \cos\theta_{proj_1} B_{ht_1} \\ \cos\theta_{hr_2} B_{hr} + \cos\theta_{proj_2} B_{ht_2} \\ \vdots \\ \cos\theta_{hr_n} B_{hr} + \cos\theta_{proj_n} B_{ht_n} \end{bmatrix} + \begin{bmatrix} b_1 \\ b_2 \\ \vdots \\ b_n \end{bmatrix}^T \begin{bmatrix} B_{vr} + B_{vt_1} \\ B_{vr} + B_{vt_2} \\ \vdots \\ B_{vr} + B_{vt_n} \end{bmatrix}\right) \tag{14}$$

with

$a_i = \frac{\sqrt{R_i^2 - H_i^2}}{R_i}$; and $b_i = \frac{H_i}{R_i}$

where a_i and b_i are measure geometry parameters, and they can be obtained for each corresponding pixel. The azimuth angle corresponding to pixel i can be expressed as $\theta_{hr} = \theta_{hr_i} - (m-1)\bullet Reso_{azi}$, where m denotes the azimuth direction index of the m th pixel on the interferogram, and $Reso_{azi}$ represents the azimuth resolution per pixel. It is also important to note that the tilting parameters are defined as parameter sets which can be calculated from tilt direction angle θ_{td}, and tilt angle θ_t. Accordingly, the phase component for pixel i can be estimated by the objective function defined in Eq. (15).

$$\hat{\phi}_i = argmin \sum_{i=1}^{n} \left(\phi_{est,i} - \phi_{obs,i}\right)^2 \tag{15}$$

Each pixel in the interferograms serves as an observation that adheres to the proposed model. We can then estimate the parameters using an iterative least-squares estimator (LS), where convergence occurs when the difference between the estimated and true phases falls below a predefined threshold, i,e., 10^{-6} in this study (Björck, 1990; Coleman and Li, 1996). It is noteworthy that the proposed joint estimation model can be extended to simultaneously address deformation and atmospheric phase screen (APS) mitigation, similar to the approach in Zhang et al. (2014). All the code for the proposed methodology will be made publicly available at https://github.com/LiuYH-InSAR/GBIR-repositioning will be released after the acceptance. The flowchart of data processing of the proposed joint estimation methods is illustrated in Fig. 3. The symbols

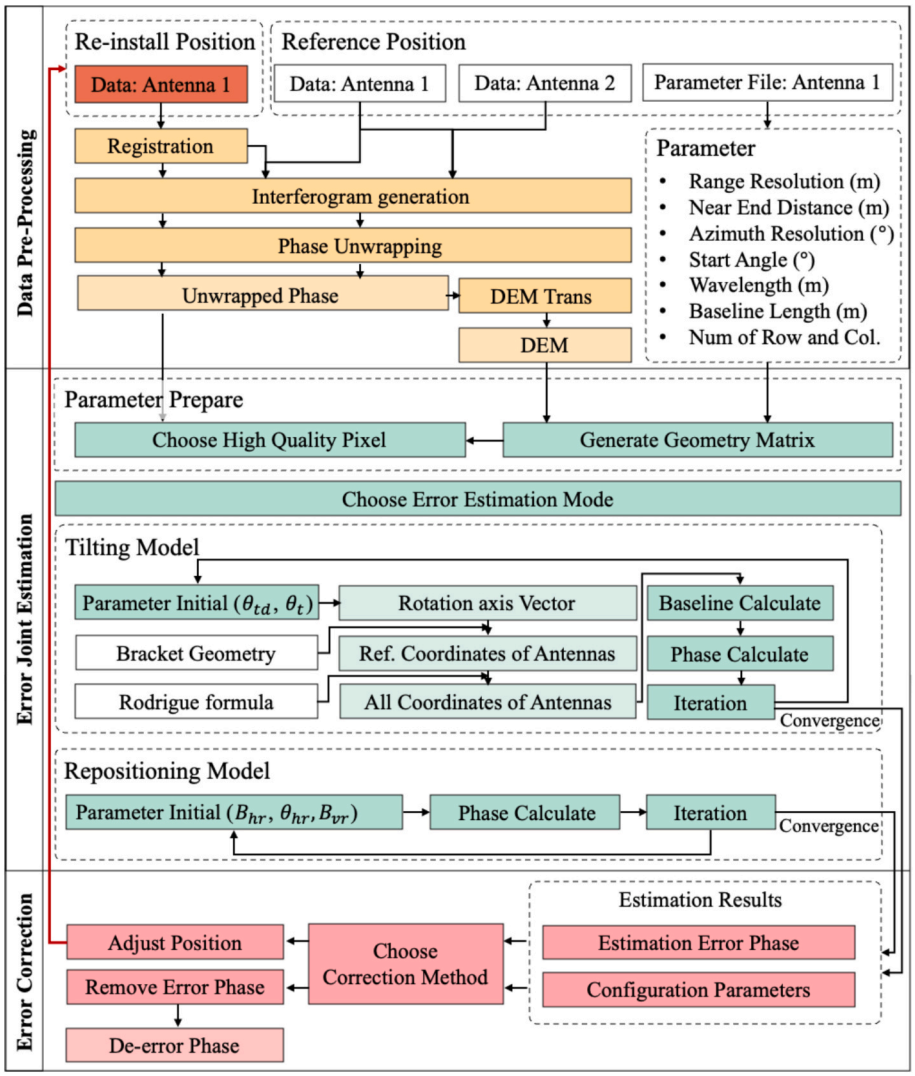

Fig. 3. The flowchart of data processing of the proposed joint estimation methods.

used in this study are listed in the Table A1 of Appendix.

4. Experiment with real GPRI-II data

In this section, we conducted two sets of field experiments and generated three datasets to evaluate the effectiveness of the repositioning error estimation, tilt error estimation, and the overall performance of the joint estimation model, respectively. Detailed information is provided in the following sections.

4.1. Study area and experiment parameters

To validate the proposed model, we select a stable north-facing slope near the Hong Kong Polytechnic University (PolyU) as the study area, see Fig. 4. The slope is characterized by a strip shape extending approximately 200 m. The GPRI-II instrument was installed on the sixth-floor platform of Block Z at PolyU to collect the datasets as shown in Fig. 4(a). The monitoring area covered a sector ranging from 50 to 500 m with a 50° azimuth span in Fig. 4(b).

To evaluate the repositioning error model, termed the first dataset, the GPRI-II was manually re-setup multiple times with different locations in both horizontal and vertical directions to simulate the repositioning error among multiple short-term monitoring scenarios. The corresponding positions are displayed in Fig. 4(c), where the sector denotes the scanned area, and the polar coordinate axis aligns with the initial angle of the sector. To evaluate the tilting error model, termed the second dataset, we fixed the instrument and adjusted the leveling mechanism within 1° in different directions to generate tilting error. The tilt angle is depicted as unit vectors within the rotation axis in Fig. 4(d). To evaluate the joint estimation model, we created a third dataset by combining the two previous datasets to generate interferograms containing both repositioning and tilting errors. It is worth noting that all re-setup parameters were measured using a total station to obtain precise positional coordinates, which were later compared with estimated values to validate model accuracy. The total station was set near the GPRI instrument to measure the locations of GPRI during the validation experiment. A target sticker was attached to the central axis of the radar bracket for measuring the GBIR position. The detailed information with the total station is introduced in Fig. S1 of the Supplementary Materials.

To reduce the influence of extraneous phase errors, such as atmospheric variations in Eq. (2), which could affect the comparion and validation of the proposed and traditional methods, all experiments were conducted within a short time window. During the data collection, the GPRI is operated at a rotation speed of 1°/s and a monitoring frequency of 500 Hz, each image was collected in approximately 1 min. Detailed RAS monitoring parameters, which remained consistent across all experiments, are provided in Table 2. On the other hand, it is confirmed that the slope is stable, no deformation signal will be evolved

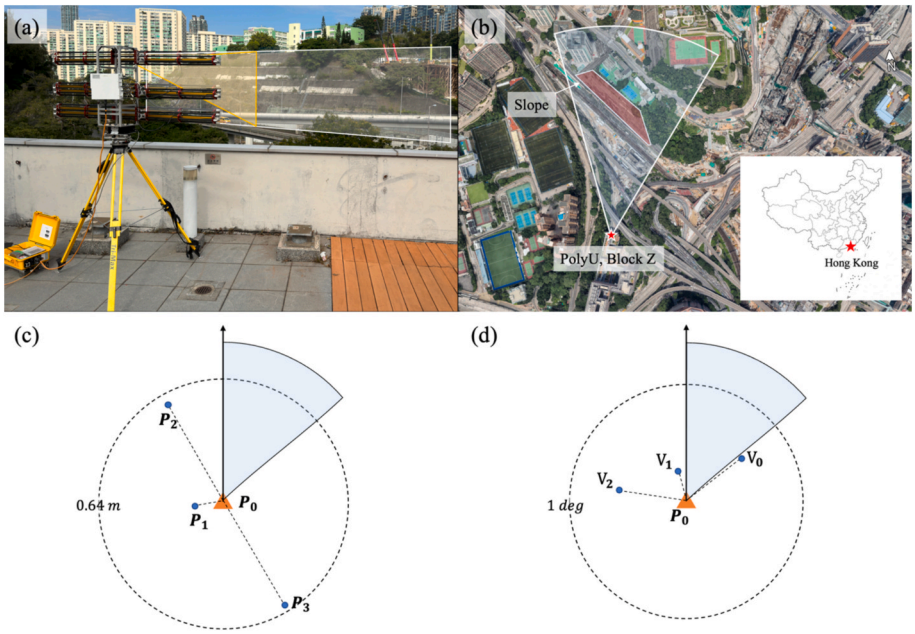

Fig. 4. The study area and position of GPRI. (a) monitoring scene (b) study area (c) position of GPRI in repositioning error verify experiment (d) tilt angle in tilting error verify experiment, where the V_0 represents the tilt angle of the master image during the experiment.

Table 2
Parameters of RAS mode in the validation experiment.

Parameters	Value
Range	50 to 1300 m
Azimuth angle	50 °
Rotating speed	1 °/s
Monitoring duration	50 s/sense
Elevation angle	0 °

in the experiments. To enhance the signal-to-noise ratio, an azimuth multi-look factor of 5 was applied in the GPRI-II during data collection. Therefore, the observed interferometric phase in Eq. (2) will only include the re-setup error and decorrelation noise component.

4.2. D-InSAR data processing

The objective of the experiments is to estimate and remove the phase errors caused by different positions and tilting angles. To achieve this, interferograms were generated by combining SLCs acquired at different positions or tilting angles. We first selected a reference SLC as the master

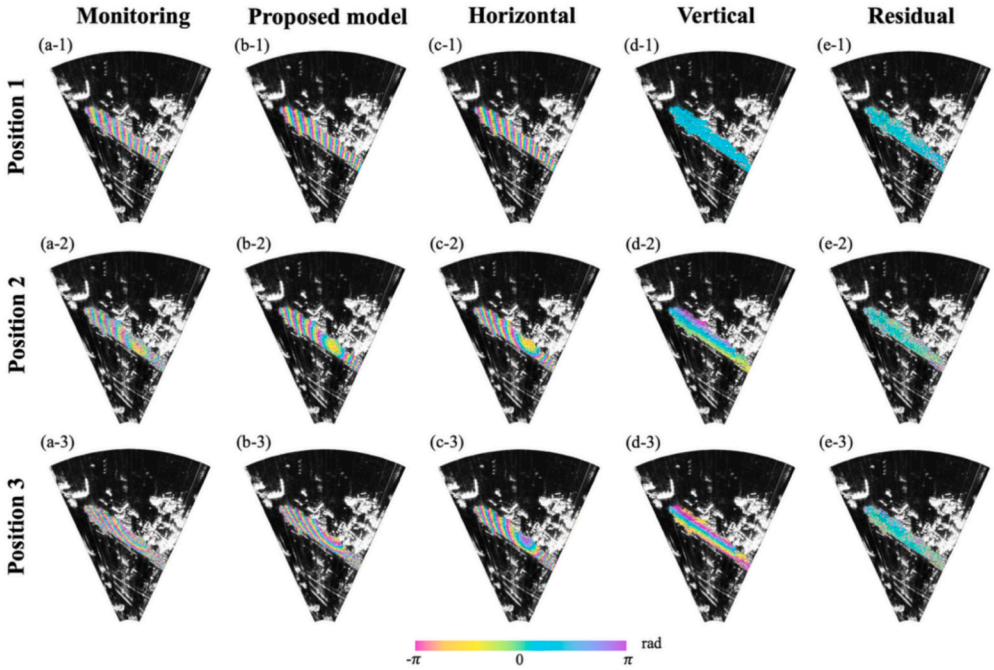

Fig. 5. Example results of repositioning error correction. (a) original interferograms, (b) estimated repositioning error phases, (c) the horizontal components of the repositioning error, (d) the vertical components of the repositioning error, (e) residual phases.

SLC and treated the other SLCs with different positions or tilting angles as slave SLC images. Each slave SLC was then coregistered to the master SLC. Subsequently, interferograms were generated, and a noise mask with a coherence threshold of 0.4 was applied to suppress potential noise that could lead to phase unwrapping errors. Finally, the interferograms were unwrapped using the Minimum Cost Flow (MCF) algorithm implemented in the GAMMA software.

4.3. Experiment results of repositioning error correction

The first dataset that only contains the repositioning error was used in this section to validate the repositioning error model in Section 3.1. The proposed repositioning error model was applied to estimate and correct the error phase based on the unwrapped phase. Some examples of experiment results are illustrated in Fig. 5. Fig. 5(a) is the original interferograms, the fringes distribute regularly on the slope related to the movements of the GPRI-II system, specifically the repositioning error phase. The bias induced by repositioning error is approximately 26π rad for a 0.15-meter baseline and 50π rad for a 0.30-meter baseline, corresponding to 2.262- and 4.350-meter deformation along the LOS direction, respectively, if not corrected. Therefore, those errors must be removed to ensure the accuracy of deformation monitoring in the future.

The model estimated phases are shown in Fig. 5(b), while the corresponding horizontal and vertical components are presented in Fig. 5 (c) and Fig. 5(d), respectively. As shown in the first two rows of Fig. 5, the phase fringes in these interferograms are primarily contributed by the horizontal component as stated in Eq. (7). Specifically, the horizontal components in the first row (Fig. 5(c-1)) exhibit uniform striping, whereas those in the second row (Fig. 5(c-2)) appear spotted. This difference is due to variations in the horizontal angle between the baseline and the monitored target, aligning with the spatial pattern observed in Fig. 2(d). Since the ground-based radar moved on a nearly flat platform, the vertical baselines are much shorter, resulting in smaller vertical component errors. These findings are also consistent with the spatial pattern of terrain changes in Fig. 2(e). The residual phases are shown in Fig. 5(e) without fringes, demonstrating the efficient mitigation and the error-correction of the proposed model. The noise signals mainly contributed by the decorrelation noise related to vegetation on the slope, as shown in Fig. 4(a).

Since the precise coordinates of the GPRI-II were measured with a total station within a local coordinate system, the measured 3D coordinates were converted to a polar coordinate system to validate the accuracy of the estimated values. The comparison between the estimated and measured baseline parameters are summarized in Table 3, revealing a high degree of agreement. The mean errors are less than 0.01 mm for the horizontal baseline (B_{hr}), 0.26 degrees for the horizontal angle (θ_{hr}), and 1.43 mm for the vertical baseline (B_{vr}). And the mean absolute errors (MAE) are 3.07 mm for the horizontal baseline (B_{hr}), 0.26 degrees for the horizontal angle (θ_{hr}), and 6.07 mm for the vertical baseline (B_{vr}). These results indicate that B_{hr} exhibits negligible systematic bias, as its mean error is nearly zero compared to its MAE. In contrast, B_{hr} shows a slight positive bias, with a mean error almost equal to its MAE, implying that the proposed model tends to overestimate θ_{hr}. For B_{vr}, the mean error is much smaller than the MAE, suggesting that both positive and negative deviations occur, which is consistent with random error characteristics. Notably, the total station, positioned within 10 m of the GPRI-II, provides an angular measurement accuracy of 5 arcseconds and a distance measurement accuracy of 3 mm, corresponding to monitoring accuracies of 5.6 mm for B_{vr}, 0.18 degrees for θ_{hr}, and 2.7 mm for B_{hr}. Therefore, these results confirm the high accuracy of the proposed model in estimating repositioning errors. Furthermore, the estimated values can be utilized for instrument reconfiguration to enhance operational performance.

4.4. Experiment results of tilting error correction

As outlined in Section 3.2, even when a fixed pile is used to re-establish the GBIR system, tilting error can still occur due to the limited accuracy of the level bubble. In this section, the second datasets are used to validate the proposed tilting error correction model. Similar to the previous section, we used the proposed model to estimate and correct the tilting error after we achieved the unwrapped interferograms.

The experiment results are illustrated in Fig. 6. The two original interferograms included the tilting error are shown in Fig. 6(a). Among them, the first and third rows display results from the lower antenna, while the second and fourth rows correspond to the upper antenna. The error phases are represented as slight signals with an azimuth trend presented in the interferograms, which typically remains within 2π and is smaller than the repositioning error. Since the upper antenna is fixed on the farther end from the rotation center, adjustments result in larger distance compared to the lower antenna. So, the interferograms from the upper antenna are more significantly affected by the tilting error as shown in Eq. (8) to Eq. (10).

To ensure more reliable results and consistent tilt angles, the phase estimation is performed using data from both antennas simultaneously. The estimated titling error phase and their corresponding horizontal and vertical components are shown in Fig. 6(b), Fig. 6(c), and Fig. 6(d), respectively. Since the rotation axis is nearly vertical and can only be adjusted within a limited range (within 1 degree), tilting error is primarily significant in horizontal components, and the error phase trend in Fig. 6(c-4&d-4) aligns well with the spatial pattern in Fig. 2(f). After correction, all error trends are mitigated in the residual phases in Fig. 6 (e).

To validate the accuracy of the proposed tilting model, we also measured the geometric changes of the GPRI-II with the total station during the experiments. Before each adjustment of the rotation axis, the radar antenna was reset to a 0° position, and all three non-collinear targets mounted on the same plane on the bracket were measured. Given that the initial rotation axis vector is assumed to be $V(0,0,1)$, which is unlikely to represent the actual, perfectly vertical rotation axis in practice, the total station measurements were transformed into the corresponding coordinate system for a more rigorous comparison. The comparison results between estimated and measured values are summarized in Table 4, demonstrating a high accuracy of the proposed tilting model. The average differences are 3.75 degrees in tilt direction angle (θ_{td}), and 0.25 degrees in the tilt angle (θ_t), which can be directly used to reconfigure the instrument to eliminate the tilt angle.

Table 3
Comparison between measured values and estimated values by repositioning model B_{hr} and B_{vr} in **mm** and rotation angle θ_{hr} in **deg.**

Group	Measured by total station			Proposed model			Difference		
	B_{hr}	θ_{hr}	B_{vr}	B_{hr}	θ_{hr}	B_{vr}	B_{hr}	θ_{hr}	B_{vr}
1	144.3	298.3	0	144.4	298.3	0.2	0.1	0	0.2
2	582.2	29.4	36.8	577.6	29.9	29.7	−4.6	0.5	−6.9
3	606.7	207.7	−76.5	611.2	208.0	−65.4	4.5	0.3	11.1
Mean							**0**	**0.26**	**1.43**
MAE							**3.07**	**0.26**	**6.07**

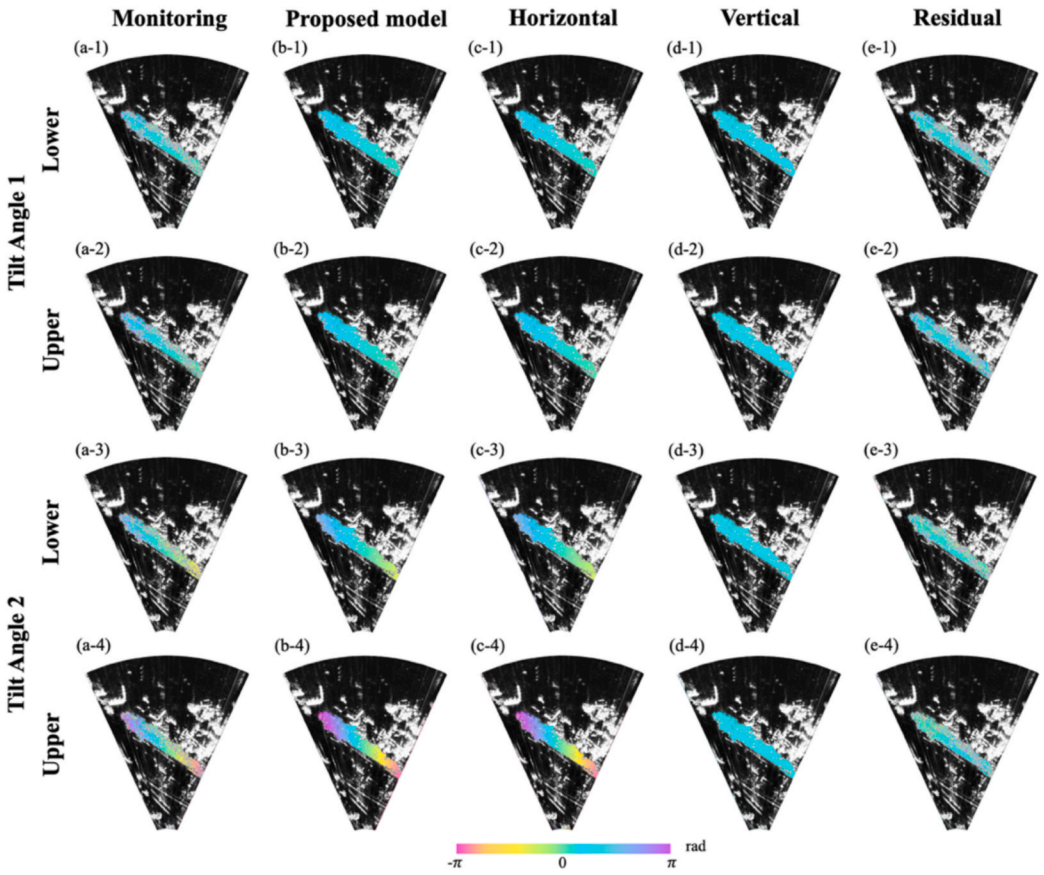

Fig. 6. Example results in tilting error correction. (a) original interferograms, (b) estimated tilting error phases, (c) the horizontal components of the tilting error, (d) the vertical components of the tilting error, (e) residual phases.

Table 4
Comparison between measured values and estimated values by the tilting model θ_{td} and θ_t in **deg**.

Group	Measured by total station		Proposed model		Difference	
	θ_t	θ_{td}	θ_t	θ_{td}	θ_t	θ_{td}
1	0.53	133.20	0.20	129.71	−0.33	−3.49
2	1.03	200.20	0.86	204.21	−0.17	4.01
Mean					**−0.25**	**0.26**
MAE					**0.25**	**3.75**

4.5. Experiment result of joint model estimation

In practical monitoring scenarios, repositioning and tilting components typically occur simultaneously, necessitating a joint estimation of the error phase. To obtain interferograms containing both repositioning and tilting errors, we generate the interferograms by using the images from the first and second datasets, termed the third datasets. Specifically, SLC images acquired at the same location as in Fig. 5(a-1) from the repositioning validation experiment was used to generate the interferogram with another image having the same tilt angle as shown in Fig. 6(a-3) and Fig. 6(a-4) from the tilting validation experiment. The resulting interferograms, along with the corresponding estimated phase and residual phase, are presented in Fig. 7. As shown in the figure, the estimated repositioning and tilting components are consistent with the results previously observed in Fig. 5(b-1), Fig. 6(b-3), and Fig. 6(b-4), respectively. The estimated reconfiguration parameters are summarized in Table 5, indicating the highly align with the measured value from the total station in the repositioning component. In terms of the accuracy of tilting error estimation, the tilt angle θ_t is 1.1°, and the tilt direction angle θ_{td} is 2.1°. It is worth noting that the estimation accuracy of the tilt angle is generally higher in the joint estimation framework than in the only-tilting estimation. This is because variations in the tilt angle can also introduce slight repositioning errors at the millimeter level, primarily caused by off-axis adjustments of the azimuth positioning instrument in the GPRI system. To obtain more accurate estimates of the phase and associated parameters, it is therefore recommended to incorporate the repositioning component into the model.

In terms of the accuracy of repositioning error estimation, the average discrepancies are 2.12 mm in the horizontal baseline (B_{hr}), 0.25° in the horizontal projection angle (θ_{hr}), and 1.07 mm in the vertical baseline (B_{vr}). It can be seen that the joint estimation model outperforms the models using only repositioning error correction or tilting error correction, as shown in Table 3, demonstrating that joint estimation can provide a reliable and practical means of assisting instrument alignment and calibration during practical monitoring. It is important to note that this section presents only the results with representative error patterns; the remaining experimental results are provided in Fig. S2 and Table S1 in the Supplementary Material. In addition, we also conducted 1,000 simulation experiments with various repositioning and tilting errors, as detailed in Tables S2 and S3 of the Supplementary material. The results demonstrate the robustness and performance of the proposed joint model in addressing arbitrary repositioning and tilting errors.

5. Discussion

5.1. Comparison experiment with existing methods

5.1.1. Repositioning error correction

In order to demonstrate the effectiveness of proposed repositioning error correction model, we conducted the three comparison experiments against to the existing methods, i.e., polynomial fitting model (Hu et al.,

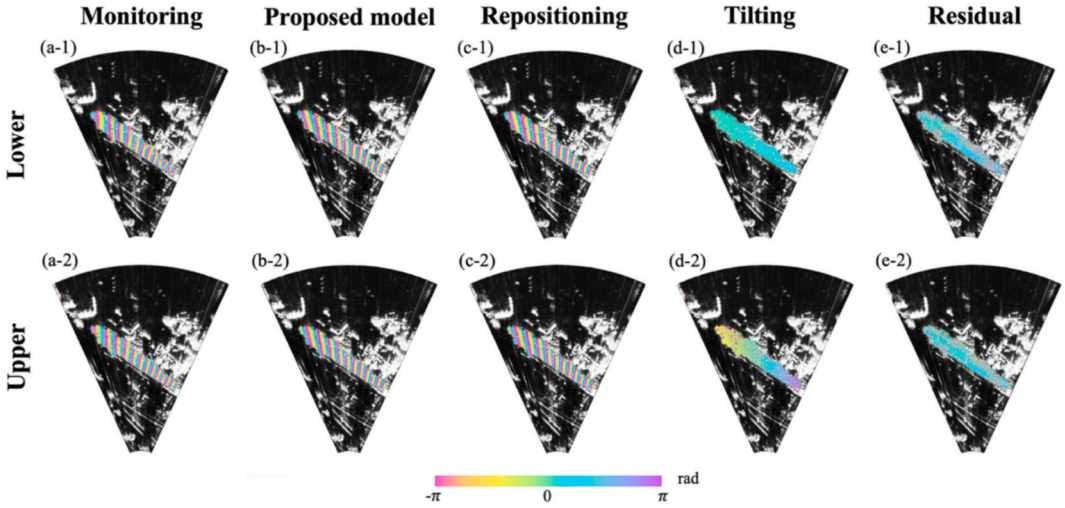

Fig. 7. Example results in joint estimation correction. (a) original interferograms, (b) estimated tilting error phases, (c) the horizontal components of the tilting error, (d) the vertical components of the tilting error, (e) residual phases.

Table 5
Comparison between measured values and estimated values by joint model θ_{td}, θ_t, θ_{hr} in **deg** and B_{hr}, B_{vr} in **mm**.

Group	θ_t	θ_{td}	B_{hr}	θ_{hr}	B_{vr}
Joint Est.	0.86	204.22	145.64	305.01	28.68
Total station	1.03	202.20	143.52	306.86	27.61
Difference	**0.17**	**2.02**	**2.12**	**0.25**	**1.07**

2021; Wang et al., 2019), and traditional model method (Mo et al., 2024). For a fair comparison, we used Fig. 5(a-1) data from Section 4.3, where the influence of the vertical baseline is minimal, with results shown in the first row of Fig. 8. The results are shown in Fig. 8, in which only the phase on the slope is illustrated for better visualization. The comparison of standard deviation (STD) values is summarized in Table 6.

Since we implemented a phase mask (coherence threshold of 0.4) to minimize the influence of extraneous phases during data processing, only pixels with phase quality higher than 0.4 coherence remained, equivalent to around 0.725 rad STD of noise level (Wu et al., 2018). Therefore, after mitigating the repositioning error phase, a smaller remaining residual indicates higher method accuracy. As shown in Fig. 8, all three methods effectively mitigate the stripe shape pattern. The average STD of the original phase was reduced from 13.1274 rad to 0.8061 rad, 0.9704 rad, and 1.6279 rad by the proposed method, polynomial fitting, and the traditional model, respectively. The

Table 6
Accuracy comparison of methods, the unit is radian (rad).

Group	IFG	Proposed method	Polynomial	Traditional model
1	20.3384	0.3561	0.3940	0.3584
2	10.3230	0.7823	0.9045	0.9193
3	8.7207	1.2798	1.6126	3.6061
Mean	13.1274	**0.8061**	0.9704	1.6279

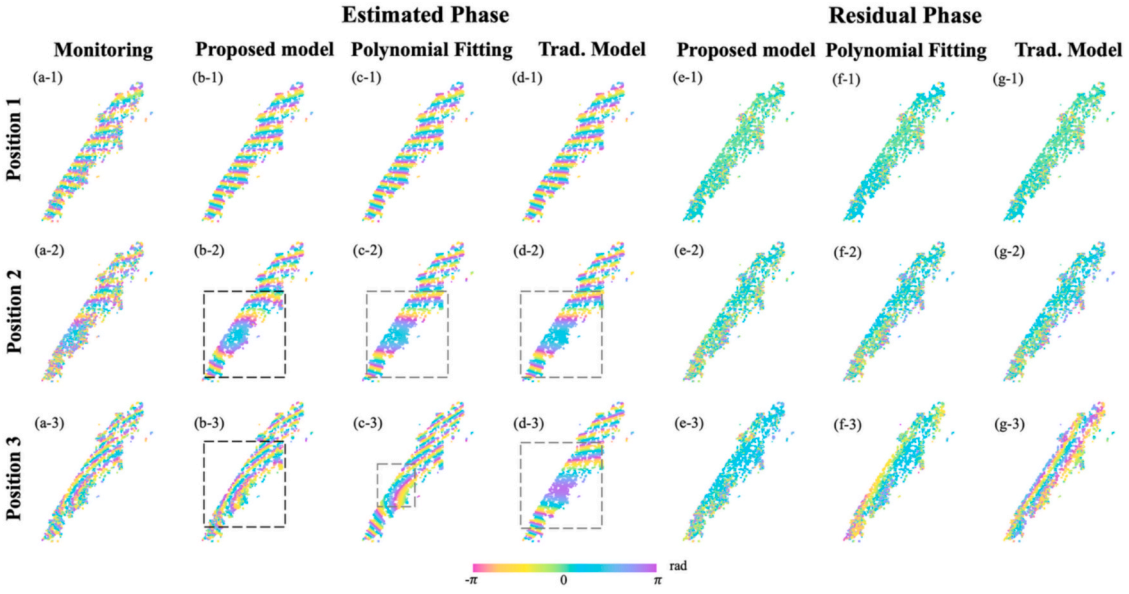

Fig. 8. Comparison of the results of the proposed repositioning model with traditional fitting methods and traditional models. (a) interferograms, (b) estimation phase of proposed method, (c) estimation phase of polynomial fitting method, (d) estimation phase of traditional model fitting method, (e) residuals of proposed method, (f) residuals of polynomial fitting method, (g) residuals of traditional model fitting method.

proposed model demonstrates an improvement of 16.93 % and 50.48 % compared to polynomial fitting and the traditional model. Furthermore, the spatial distribution of the signal demonstrates that the proposed model more effectively removes errors of various fringe shapes than the other methods.

5.1.2. Tilting error correction

Similar to the previous section, we evaluated the effectiveness of the proposed tilting error correction model and compared it with these two traditional methods. The comparison results are shown in Fig. 9 and the STD values are summarized in Table 7. As the spatial pattern, all three kinds of methods can well restore the fringe characteristics of the original monitoring data in most areas. However, the polynomial fitting and traditional model may retrieve the wrong spatial pattern, as shown in Fig. 9(c-1) and Fig. 9(d-1), which are inconsistent with the pattern in the observed interferogram in Fig. 9(a-1). The proposed model can be calculated jointly by the results of the upper and lower antennas, so it has higher robustness and accuracy. In addition, since the trends that the three models can fit are different, the estimated phases may also have numerical differences, as shown in Fig. 9(b), Fig. 9(c), and Fig. 9(d)). The average STD values of the proposed method is 0.7625 rad with 10.87 % (0.8555 rad) and 10.66 % (0.8535 rad) improvement when compared to polynomial fitting and traditional model, respectively, in Table 7.

5.1.3. Joint model estimation

To evaluate the effectiveness of the proposed joint estimation method, an interferogram containing both repositioning and tilting errors was generated using the same interferograms as in Section 4.5. As these errors exhibit similar phase patterns (see Figs. 2d and 2f), relying solely on the repositioning model may inadvertently compensate for

Table 7
Accuracy analysis of the tilting error model, the unit is radian (rad).

Group	IFG	Proposed method	Polynomial	Traditional model
1	0.8086	0.7074	0.7867	0.7858
2	1.4415	0.8175	0.9242	0.9212
mean	1.1250	**0.7625**	0.8555	0.8535

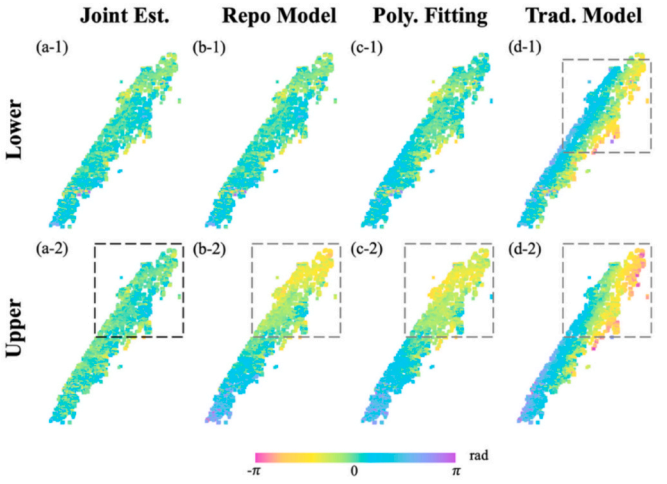

Fig. 10. Residual comparison between joint estimation and other method. (a) joint estimation, (b) repositioning component estimation, (c) polynomial fitting method, (d) traditional model.

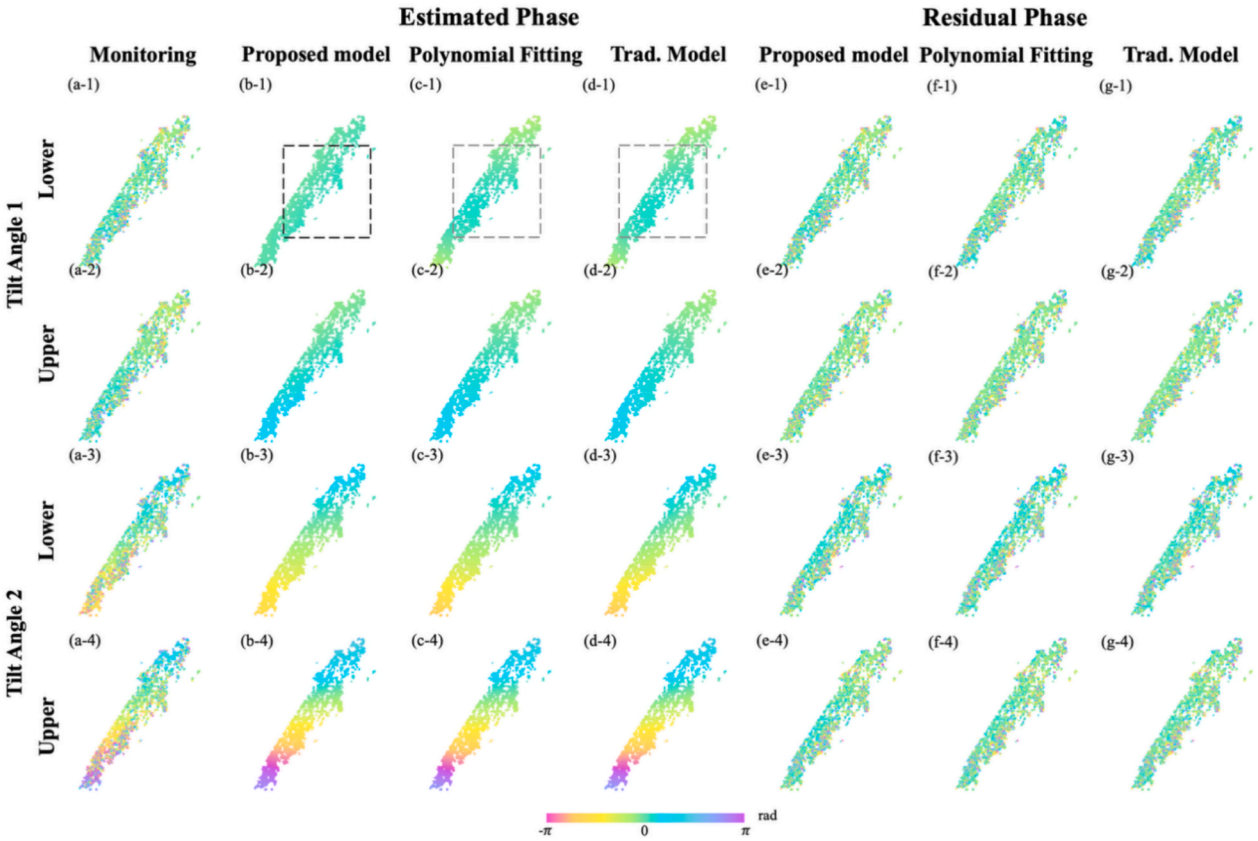

Fig. 9. Comparison results between the proposed tilting error correction model, polynomial fitting, and traditional model fitting methods. (a) original interferograms, (b) estimated phase of proposed method, (c) estimated phase of polynomial fitting method, (d) estimated phase of traditional model fitting method, (e) residuals of proposed method, (f) residuals of polynomial fitting method, (g) residuals of traditional model fitting method.

Table 8
Accuracy analysis of joint estimation, the unit is radian (rad).

Group	Antenna	IFG	Joint estimation	Repositioning model	Polynomial fitting	Traditional model
1	lower	20.5719	**0.6962**	1.0133	1.0604	1.3749
	upper	21.1254	**0.7369**	1.0367	1.0652	1.3859
mean		20.8487	**0.7165**	1.0250	1.0628	1.3804

both error types. For a comprehensive comparison, the proposed joint estimation method, which simultaneously estimates repositioning and tilting components, was benchmarked against the repositioning-only model, polynomial fitting, and the traditional model. The resulting interferograms and the corresponding estimation phases and residual phases are shown in Fig. 10, and the STD values are shown in Table 8.

The joint model demonstrated superior detrending performance. This improvement is attributed to the fact that other methods consider only a single error component, which may lead to estimation inaccuracies. The STD values of all four methods are 0.7165 rad, 1.0250 rad, 1.0628 rad, and 1.3804 rad, respectively. Moreover, in practical monitoring scenarios, if the tilting error is ignored and the same repositioning error estimate is used to correct both the upper and lower antenna data, more residuals may remain in the upper antenna. This is supported by the fact that the estimated baseline parameters for the upper and lower antennas at the same GPRI position differ, as shown in Table 9. In contrast, the joint estimation method accounts for this effect and achieves better error correction for both antennas simultaneously. Moreover, we also conducted the simulation experiments, as shown in Supplementary material, to compare with traditional models in Table S3, S4, S5 and S6, which indicating the robust accuracy of proposed joint model across different scenarios.

5.2. Determining the upper bound of re-setup error tolerance

Since the proposed model estimates reconfiguration parameters based on the unwrapped phase, the decorrelation or phase unwrapping errors can reduce the estimation accuracy, particularly when the large re-setup errors raised a denser phase fringe (see Section 4.3). To determine the upper bound of re-setup error tolerance for the proposed model, a decoherent model is established to better guidance of the deployment the GPRI-II system. Inspired by the spaceborne InSAR, the decorrelation effect is related to the spatial decorrelation (baseline length B) and the 'zero' coherence value ($\gamma = 0$) represents as the decoherent. Therefore, a formula is used to indicate the critical baseline B_c and the satellite geometry, as shown in Eq. (16) and Eq. (17). the critical baseline related to (Zebker and Villasenor, 1992).

$$\gamma = 1 - \frac{2|B| Reso_{range} cos^2\theta_{inc}}{\lambda r} \tag{16}$$

$$B_c = \frac{\lambda r}{2 R_{range} cos^2\theta_{inc}} \tag{17}$$

where λ is radar wavelength, $|B|$ is the length of baseline, r is slant distance between satellite and target, $Reso_{range}$ repersents the resolution along range direction, and θ_{inc} stands for the incident angle.

The decoherent related to denser phase fringes can be considered that the difference between adjacent resolution pixels exceeding π will lead to the unwrapping errors (Domínguez-Guzmán et al., 2009). Compared with spaceborne InSAR systems, GBIR systems typically operate with smaller incidence angles, resulting in a different observation geometry. As a consequence, decorrelation effects in both the azimuth and range directions need to be taken into account.

Based on the proposed model, we conducted separate simulation experiments for the azimuth and range directions. Specifically, for the azimuth direction, we investigated the relationship between the decorrelation angle and horizontal baseline length. For the range direction, we studied the relationship between the monitoring range, target incident angle, and vertical baseline. The resulting empirical formulas for the critical baselines of the GPRI were obtained through curve fitting of the simulation results.

In the azimuth direction, as shown in Fig. 11(a), the range of

Table 9
The estimated repositioning reconfiguration parameters of joint estimation and separate estimation, θ_{hr} in **deg** and B_{hr}, B_{vr} in **mm**.

Group	antenna	B_{hr}	θ_{hr}	B_{vr}
Repo. estimation	lower	148.49	304.48	27.01
	upper	153.44	305.35	27.99
Joint estimation	whole	145.64	305.01	28.68
Total station	whole	143.52	306.86	27.61

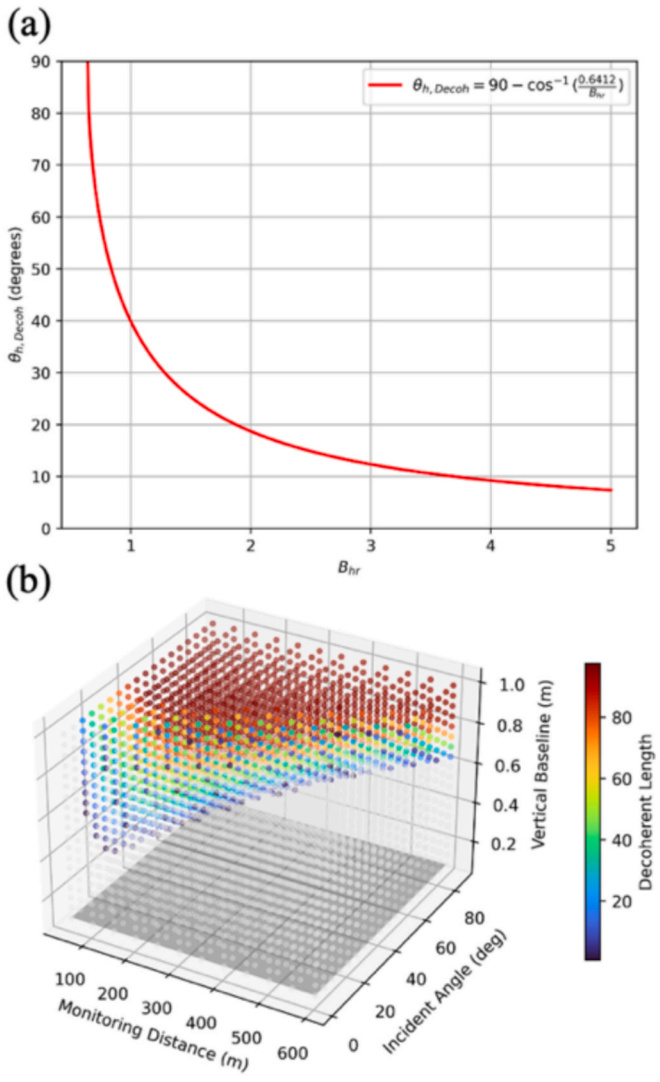

Fig. 11. The critical baseline of GPRI radar. (a) the relationship between critical baseline in vertical direction and azimuth angle (b) the relationship between critical baseline in vertical direction to monitoring range and incident angle of the target.

decorrelation is typically related to the azimuth angle θ_{hr}. The relationship between the decoherence angle θ_{h_Decoh} in the horizontal direction and the horizontal baseline B_{hr}, can be described with an empirical formula in Eq. (18).

$$\begin{cases} \theta_{h\_Decoh} > 90 - arccos\left(\dfrac{0.64}{B_{hr}}\right) & 90^{\circ} > \theta_{hr} \geq 0^{\circ} \\ \theta_{h\_Decoh} \leq 90 - arccos\left(\dfrac{0.64}{B_{hr}}\right) & 180^{\circ} > \theta_{hr} \geq 90^{\circ} \\ \theta_{h\_Decoh} > 270 - arccos\left(\dfrac{0.64}{B_{hr}}\right) & 270^{\circ} > \theta_{hr} \geq 180^{\circ} \\ \theta_{h\_Decoh} \leq 270 - arccos\left(\dfrac{0.64}{B_{hr}}\right) & 360^{\circ} > \theta_{hr} \geq 270^{\circ} \end{cases} \tag{18}$$

From the Eq. (18), decorrelation is more sensitive to the azimuth direction, especially at 90 ° and also 270 °, which is consistent with the spatial distribution observed in Fig. 2(d). As the length of the horizontal baseline increases, the range affected by decoherence increases. The change of the decoherence azimuth angle is intuitively shown in Fig. 11 (a). Moreover, according to the empirical formula in Eq. (18), no decorrelation occurs when the horizontal baseline is below 0.64 m.

In the range direction, the degree of decorrelation is influenced by terrain, monitoring distance, and the vertical baseline (Li, 2022). Based on the decorrelation criteria mentioned above, a simulation was conducted to derive the empirical relationship between the vertical baseline and both terrain slope and monitoring distance under the condition of critical decorrelation. Fig. 11(b) illustrates the proportion of decorrelated pixels in a 100 m-high building under different vertical baseline lengths, monitoring distances, and incident angles. Gray dots indicate cases without decorrelation. The critical points where decorrelation first occurs were selected for surface fitting, resulting in the critical baseline surface, and the corresponding empirical formula is presented in Eq. (19). The critical baseline in the vertical direction $B_{v_{Decoh}}$ varies with the monitoring distance D and incident angle θ_{inc}. For a building with a monitoring range of 200 m and a height of 100 m, the vertical critical baseline is 0.30 m.

$$B_{v_{Decoh}} > 0.6236 + 0.0031D - 0.0211\theta_{inc} - 2.263 \times 10^{-7} \times D^2 + 1.8691 \times 10^{-4} \times {\theta_{inc}}^2 - 2.66 \times 10^{-5} \times D \times \theta_{inc} \tag{19}$$

To verify the decoherent model, we selected an example interferogram with partial decoherence region as shown Fig. 12(a). The interferogram has a 1.68 m horizontal baseline and a span from 183 ° to 223 °, with almost no vertical baseline. Based on those parameters, we simulated the decoherence area based on the decoherent model and compared with the real interferogram as shown in Fig. 12. It can be seen from the simulated result, the decoherence area under this baseline parameter is from 202 ° to 223 °, which covers part of the image. The decoherence index is consistent with the decoherence region in Fig. 12(b), indicating the effectiveness of the proposed decoherence model for GPRI-II system.

In practical monitoring scenarios, additional decoherence factors, such as temporal decoherence and thermal noise, must be considered. To ensure high-quality interferometric images, it is recommended to use baseline parameters significantly smaller than the critical baseline. Notably, GBIR systems are typically equipped with a GPS sensor that provides positional accuracy ranging from centimeters to one decimeter. By properly utilizing the equipped GPS to guide instrument re-setup, the re-setup error will easily be remained within the upper bound of error tolerance. Therefore, the proposed model will perform reliably and effectively in practical applications.

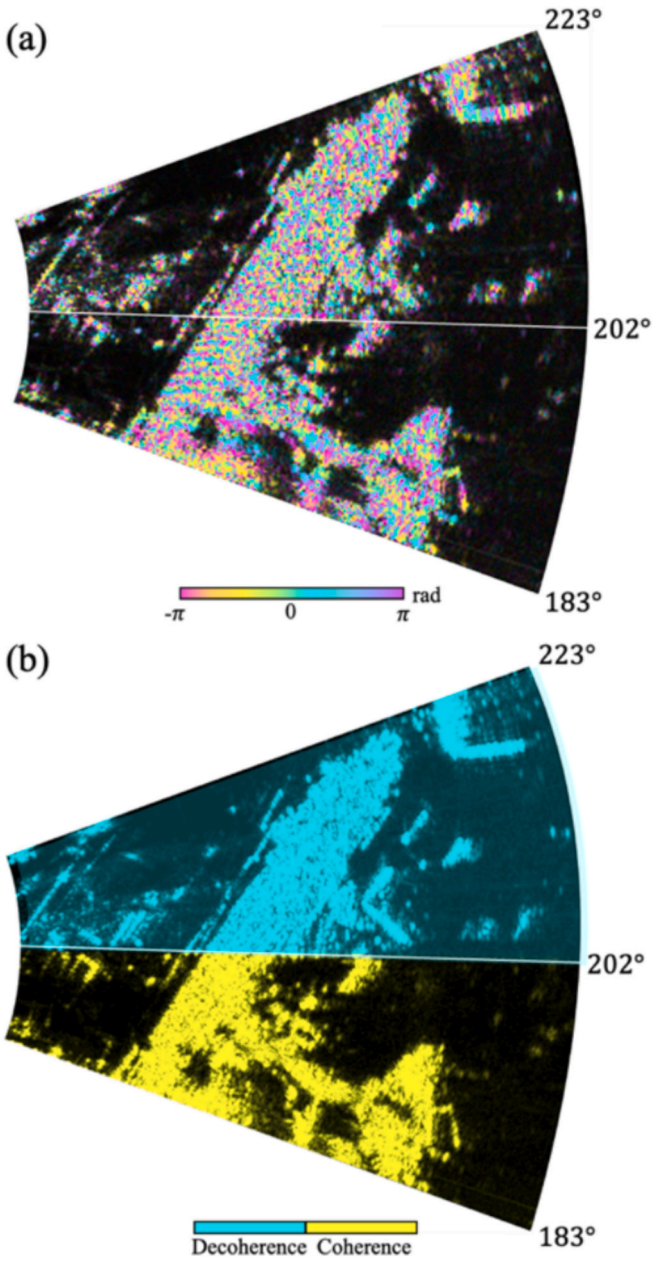

Fig. 12. The calculated critical baseline in the monitoring scenarios. (a) interferograms (b) corresponding decoherence index.

5.3. Limitations and future work

Although the proposed model effectively estimates three-dimensional re-setup errors for GPRI-II system reconfiguration and phase error mitigation, which is critical for long-term deformation monitoring, it still has certain limitations. The accuracy of the DEM phase is crucial to our methodology, as noted in prior studies. Inaccuracies in the DEM generated by GPRI interferometry can impair error estimation, leading to unreliable results. The relatively small baseline, typically 0.25 m or 0.60 m, combined with the sensitivity of Ku-band used by GPRI-II to vegetation, can degrade DEM quality and cause erroneous estimations. To address this limitation, we can incorporate external DEM data or apply advanced filtering techniques to enhance

DEM accuracy. Second, the proposed tilting error estimation model is computationally intensive, requiring substantial processing resources. This may restrict its applicability in scenarios involving large datasets from multiple monitoring sections. To address this problem, we will optimize the algorithm by implementing parallel processing or simplifying the computational framework without compromising accuracy. Third, in application of long-term deformation monitoring, factors such as atmospheric delay and systemically deformation can introduce error phases with trends that may interfere with baseline error estimation. To improve both spatial baseline error estimation and the mitigation of other error sources, we can extend the joint model by including the deformation and atmospheric delay in Eq. (13), which will represent a promising avenue for future research. This approach could also enhance the accuracy and reliability of deformation extraction.

6. Conclusion

This study presents a novel methodology to mitigate re-setup errors in discontinuous GPRI-II deformation monitoring. We redefined the re-setup errors into the repositioning and tilting components and modeled them separately within a polar-coordinate framework to capture their three-dimensional spatial characteristics. To enhance reliability, these error components are integrated into a unified joint estimation process to achieve the superior accuracy in error correction. The estimated parameters not only eliminate repositioning errors but also enable precise correction of the geometric attitude of the GBIR system, facilitating instrument reconfiguration. In addition, the upper bounds of error tolerance are established to guide practical deployments and ensure robust interferometric measurements. Three real-world experiments were conducted on a stable slope near the Hong Kong Polytechnic University to validate the effectiveness of the proposed methodology, demonstrating significant improvements over polynomial fitting and traditional approaches. The main contributions of this study include,

(1). To address the challenge of spatial baseline errors caused by repeated installations of ground-based interferometric radar in long-term deformation monitoring, an experiment was conducted to quantitatively investigate these errors, achieving an average standard deviation of 0.8061 rad (equivalent to 1.12 mm deformation error), with improvements of 16.93 %, and 50.48 % over the polynomial fitting and traditional model, respectively. As a type of real aperture radar, repositioning and tilting errors exist and can cause phase errors during rotated azimuth scanning mode monitoring. A joint model was proposed to estimate both GPRI-II repositioning and tilting errors for the first time, enabling the derivation of corrected deformation values.

(2). The joint estimation method outperforms existing approaches, achieving an average standard deviation of 0.7165 rad (equivalent to 0.99 mm deformation error), with improvements of 30.10 %, 32.58 %, and 48.09 % over the repositioning-only model, polynomial fitting, and traditional model, respectively, in phase error correction accuracy.

(3). For the first time, the proposed model enables precise instrument reconfiguration with accuracies of 3.07 mm (horizontal), 6.07 mm (vertical), and 0.20° (horizontal angle). Additionally, upper bounds of error tolerance (0.64 m horizontal, 0.30 m vertical) are established to guide instrument deployments, ensuring reliable interferometric measurements without decorrelation in practical applications.

In summary, the proposed model is very effective for discontinuous monitoring applications, can be extended to various radar systems, and can adapt to different configurations to correct the errors of discontinuous observations and significantly improve the deformation monitoring accuracy.

CRediT authorship contribution statement

Yuhao Liu: Writing – review & editing, Writing – original draft, Visualization, Validation, Methodology, Formal analysis, Data curation. **Zeyu Zhang:** Validation, Data curation. **Songbo Wu:** Writing – review & editing, Writing – original draft, Visualization, Validation, Supervision, Software, Resources, Methodology, Investigation, Formal analysis, Data curation, Conceptualization. **Xiaoli Ding:** Supervision, Resources, Project administration, Funding acquisition, Formal analysis. **Guoqiang Shi:** Supervision, Methodology, Investigation, Formal analysis. **Zhendong Zhang:** Validation, Formal analysis, Data curation. **Mahmoud Abdallah:** Validation, Data curation. **Bochen Zhang:** Supervision, Resources.

Declaration of competing interest

The authors declare that they have no known competing financial interests or personal relationships that could have appeared to influence the work reported in this paper.

Acknowledgement

The research was jointly supported by the National Natural Science Foundation of China (Grants No.42330717; Grant No. 42504044; Grant No.42304052), the Research Grants Council (RGC) of the Hong Kong Special Administrative Region (Grant No.15231822; Grant No.15234423; Grant No.15229523; Grant No. 25202125), and the University Grants Council of the Hong Kong Polytechnic University (P0050333; P0042898).

Appendix

Table-A1. Symbol Table.

Symbol	Variable Name
ϕ	interferometric phase
ϕ_{topo}	topographic phase
ϕ_{flat}	flat-earth phase
ϕ_{defo}	deformation phase
ϕ_{atmo}	atmospheric delay phase
ϕ_{noise}	noise phase
R	slant range
H	relative height between radar and target
λ	wavelength
B_p	perpendicular baseline
B_{hr}	horizontal baseline
B_{vr}	vertical baseline

(*continued on next page*)

(*continued*)

Symbol	Variable Name
θ_{hr}	horizontal angle
ϕ_{joint}	joint estimation error phase
ϕ_{Repo}	repositioning error phase
ϕ_{tilt}	tilting error phase
B_{repo}	repositioning baseline
$B_{\|\|}$	parallel baseline
θ_{proj}	projection angle
θ_{td}	tilt direction angle
θ_t	tilt angle
V_0	reference rotation axis vector
V	rotation axis vectors
$A_{i,j,k}$	antenna geometry centers
θ_r	scanning angle
B_{tilt}	tilting baseline
B_{ht}	horizontal baseline in tilting error
B_{vt}	vertical baseline in tilting error
$Reso_{azi}$	resolution in azimuth direction
$Reso_{range}$	resolution in range direction
γ	coherence
$\|B\|$	baseline length
θ_{inc}	incident angle
B_c	critical baseline
θ_{h_Decoh}	decoherence angle
$B_{v_{Decoh}}$	vertical critical baseline
D	monitoring distance

Appendix A. Supplementary data

Supplementary data to this article can be found online at https://doi.org/10.1016/j.isprsjprs.2025.10.010.

References

Björck, Å., 1990. Least squares methods. Handb. Numer. Anal. 1, 465–652.

Cao, W., Mao, Y., Wei, L., He, L., Zhao, Z., 2021. Atmospheric phase screen compensation of GB-SAR in deep dagushan open-pit mine. IEEE Geosci. Remote Sens. Lett. 19, 1–5.

Coleman, T.F., Li, Y., 1996. An interior trust region approach for nonlinear minimization subject to bounds. SIAM J. Optim. 6, 418–445.

Crosetto, M., Monserrat, O., Luzi, G., Cuevas-González, M., Devanthéry, N., 2014. Discontinuous GBSAR deformation monitoring. ISPRS J. Photogramm. Remote Sens. 93, 136–141. https://doi.org/10.1016/j.isprsjprs.2014.04.002.

Dematteis, N., Luzi, G., Giordan, D., Zucca, F., Allasia, P., 2017. Monitoring Alpine glacier surface deformations with GB-SAR. Remote Sens. Lett. 8, 947–956.

Domínguez-Guzmán, G., Castillo-Mixcóatl, J., Beltrán-Pérez, G., Muñoz-Aguirre, S., 2009. Itoh algorithm to unwrap 2D phase, in: García Torales, G., Flores Núñez, J.L., Gómez Rosas, G., Rosas, E. (Eds.), . Presented at the Seventh Symposium on Optics in Industry, Guadalajara, Jalisco, Mexico, p. 74990H. DOI: 10.1117/12.851057.

Herrera, G., Fernández-Merodo, J., Mulas, J., Pastor, M., Luzi, G., Monserrat, O., 2009. A landslide forecasting model using ground based SAR data: The Portalet case study. Eng. Geol. 105, 220–230.

Hu, C., Zhu, J., Deng, Y., Tian, W., Yin, P., 2021. Repositioning Error Compensation in Discontinuous Ground-Based SAR Monitoring. Remote Sens. (Basel) 13, 2461. https://doi.org/10.3390/rs13132461.

Izumi, Y., Frey, O., Baffelli, S., Hajnsek, I., Sato, M., 2021. Efficient approach for atmospheric phase screen mitigation in time series of terrestrial radar interferometry data applied to measure glacier velocity. IEEE J. Sel. Top. Appl. Earth Obs. Remote Sens. 14, 7734–7750.

Kobayashi, T., Miyahara, B., 2020. InSAR for Deformation Monitoring, in: Sideris, M.G. (Ed.), Encyclopedia of Geodesy. Springer International Publishing, Cham, pp. 1–5. DOI: 10.1007/978-3-319-02370-0_5-1.

Li, G., 2022. InSAR terrain mapping error sources based on satellite interferometry. Open Phys. 20, 668–679.

Liu, B., Ge, D., Li, M., Zhang, L., Wang, Y., Zhang, X., 2016. Using GB-SAR technique to monitor displacement of open pit slope. Presented at the 2016 IEEE International Geoscience and Remote Sensing Symposium (IGARSS), IEEE, pp. 5986–5989.

Liu, Y., Wu, S., Zhang, B., Peng, Z., Zhang, J., Wang, C., Tu, W., Chen, Z., Jiang, M., Cheng, X., 2025. Multi-dimensional dynamic deformation monitoring of long-span railway bridges using GBIR and IVM data fusion. Geo-spatial Inf. Sci. 1–17.

Luo, X., Schaufler, S., Carrera, M., Celebi, I., 2018. High-precision RTK positioning with calibration-free tilt compensation. In: Presented at the Proceedings of the FIG Congress, pp. 1–17.

Luzi, G., Pieraccini, M., Mecatti, D., Noferini, L., Macaluso, G., Tamburini, A., Atzeni, C., 2007. Monitoring of an alpine glacier by means of ground-based SAR interferometry. IEEE Geosci. Remote Sens. Lett. 4, 495–499.

Mo, Y., Lai, T., Wang, Q., Huang, H., 2024. A novel methodology for D-GBSAR repositioning error compensation based on maximum likelihood estimation. IEEE Trans. Geosci. Remote Sens.

Monserrat, O., Crosetto, M., Luzi, G., 2014. A review of ground-based SAR interferometry for deformation measurement. ISPRS J. Photogramm. Remote Sens. 93, 40–48.

Noferini, L., Mecatti, D., Macaluso, G., Pieraccini, M., Atzeni, C., 2009. Monitoring of Belvedere Glacier using a wide angle GB-SAR interferometer. J. Appl. Geophys. 68, 289–293.

Noferini, L., Pieraccini, M., Mecatti, D., Macaluso, G., Atzeni, C., Mantovani, M., Marcato, G., Pasuto, A., Silvano, S., Tagliavini, F., 2007. Using GB-SAR technique to monitor slow moving landslide. Eng. Geol. 95, 88–98. https://doi.org/10.1016/j.enggeo.2007.09.002.

Noll, M.L., Rydlund, P.H., 2020. Procedures and best practices for trigonometric leveling in the US Geological Survey (No. 2328–7055). US Geological Survey.

Qiu, Z., Jiao, M., Jiang, T., Zhou, L., 2020. Dam structure deformation monitoring by GB-InSAR approach. IEEE Access 8, 123287–123296.

Rodrigues, O., 1840. Des lois géométriques qui régissent les déplacements d'un système solide dans l'espace, et de la variation des coordonnées provenant de ces déplacements considérés indépendamment des causes qui peuvent les produire. Journal de mathématiques pures et appliquées 5, 380–440.

Su, Y., Yang, H., Peng, J., Liu, Y., Zhao, B., Shi, M., 2022. A novel near-real-time GB-InSAR slope deformation monitoring method. Remote Sens. (Basel) 14, 5585.

Wang, Z., Li, Z., Mills, J., 2019. Modelling of instrument repositioning errors in discontinuous Multi-Campaign Ground-Based SAR (MC-GBSAR) deformation monitoring. ISPRS J. Photogramm. Remote Sens. 157, 26–40. https://doi.org/10.1016/j.isprsjprs.2019.08.019.

Werner, C., Strozzi, T., Wiesmann, A., Wegmüller, U., 2008. GAMMA's portable radar interferometer. Presented at the Proc. 13th FIG Symp. Deform. Meas. Anal, pp. 1–10.

Wolff, C., Derron, M.-H., Rivolta, C., Jaboyedoff, M., 2024. A tool for estimating ground-based InSAR acquisition characteristics prior to monitoring installation and survey and its differences from satellite InSAR. Geosci. Instrum. Methods Data Syst. 13, 225–248.

Wu, S., Zhang, B., Ding, X., Zhang, L., Zhang, Z., Zhang, Z., 2023. Radar Interferometry for Urban Infrastructure Stability Monitoring: From Techniques to Applications. Sustainability 15, 14654.

Wu, S., Zhang, L., Ding, X., Perissin, D., 2018. Pixel-wise MTInSAR estimator for integration of coherent point selection and unwrapped phase vector recovery. IEEE Trans. Geosci. Remote Sens. 57, 2659–2668.

Xiang, X., Chen, J., Wang, H., Pei, L., Wu, Z., 2019. PS Selection Method for and Application to GB-SAR Monitoring of Dam Deformation. Adv. Civ. Eng. 2019, 8320351.

Yang, H., Cai, J., Peng, J., Wang, J., Jiang, Q., 2017. A correcting method about GB-SAR rail displacement. Int. J. Remote Sens. 38, 1483–1493. https://doi.org/10.1080/01431161.2017.1280631.

Zebker, H.A., Villasenor, J., 1992. Decorrelation in interferometric radar echoes. IEEE Trans. Geosci. Remote Sensing 30, 950–959. https://doi.org/10.1109/36.175330.
Zhang, B., Ding, X., Werner, C., Tan, K., Zhang, B., Jiang, M., Zhao, J., Xu, Y., 2018. Dynamic displacement monitoring of long-span bridges with a microwave radar interferometer. ISPRS J. Photogramm. Remote Sens. 138, 252–264. https://doi.org/10.1016/j.isprsjprs.2018.02.020.
Zhang, L., Ding, X., Lu, Z., Jung, H.-S., Hu, J., Feng, G., 2014. A Novel Multitemporal InSAR Model for Joint Estimation of Deformation Rates and Orbital Errors. IEEE Trans. Geosci. Remote Sensing 52, 3529–3540. https://doi.org/10.1109/TGRS.2013.2273374.